

# Local B<sub>0</sub> Shim Array Integrated onto a Solenoid TRX Coil for Permanent Magnet Scanners

*Rafael Calleja  
Celine Veys  
Michael Lustig*



Electrical Engineering and Computer Sciences  
University of California, Berkeley

Technical Report No. UCB/EECS-2021-84

<http://www2.eecs.berkeley.edu/Pubs/TechRpts/2021/EECS-2021-84.html>

May 14, 2021

Copyright © 2021, by the author(s).  
All rights reserved.

Permission to make digital or hard copies of all or part of this work for personal or classroom use is granted without fee provided that copies are not made or distributed for profit or commercial advantage and that copies bear this notice and the full citation on the first page. To copy otherwise, to republish, to post on servers or to redistribute to lists, requires prior specific permission.

### Acknowledgement

I wish to thank Professor Michael Lustig for the opportunity to work in his lab and invaluable guidance and support throughout the duration of this project.

A very special thank you to my collaborator Celine Veys. This project would not be possible without her contributions to and testing of all the complex hardware as well as the tireless hours spent on our joint collaborative efforts.

Finally, I would like to acknowledge my parents, Daniel Valentine and Maria Carmelita Calleja, as well as my siblings, Nikka and Miguel Calleja, for their unconditional support of my studies and wellbeing.

Local  $B_0$  Shim Array Integrated onto a Solenoid TRX Coil for Permanent Magnet Scanners

by

Rafael Calleja

A thesis submitted in partial satisfaction of the

requirements for the degree of

Master of Science

in

Electrical Engineering Computer Science

in the

Graduate Division

of the

University of California, Berkeley

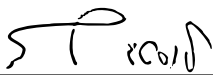
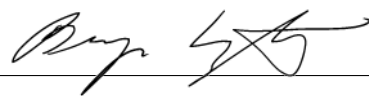
Committee in charge:

Professor Michael Lustig, Chair

Professor Vladimir Stojanovic

Spring 2021

The thesis of Rafael Calleja, titled Local  $B_0$  Shim Array Integrated onto a Solenoid TRX Coil for Permanent Magnet Scanners, is approved:

Chair Michael Lustig  Date 05/13/2021  
 Date 05/13/2021  
\_\_\_\_\_ Date \_\_\_\_\_

University of California, Berkeley

Local  $B_0$  Shim Array Integrated onto a Solenoid TRX Coil for Permanent Magnet Scanners

Copyright 2021

by

Rafael Calleja

## Abstract

Local  $B_0$  Shim Array Integrated onto a Solenoid TRX Coil for Permanent Magnet Scanners

by

Rafael Calleja

Master of Science in Electrical Engineering Computer Science

University of California, Berkeley

Professor Michael Lustig, Chair

In the realm of MRI machines, low-to-mid field systems (e.g. permanent magnet scanners) have been nearly abandoned for high-field, high-performance systems (e.g. superconducting scanners). However, recent improvements in MR hardware, algorithms and computation are stimulating a resurgence in interest of upgrading lower-end magnets to achieve high-performance with significantly lower cost, greater accessibility, and more relaxed siting requirements. Towards this goal, we propose an upgrade for a wrist 1T permanent-magnet system in the form of a simple  $B_0$  shim array integrated onto a solenoid TRX coil for reducing  $B_0$  through localized targeted shimming. We demonstrate improved homogeneity using a 16-channel prototype array with negligible effects on the transmit field and received SNR.

# Contents

<b>Contents</b>	<b>i</b>
<b>List of Figures</b>	<b>iii</b>
<b>1 Introduction</b>	<b>1</b>
1.1 Motivation . . . . .	1
1.2 Related Work . . . . .	2
<b>2 Background</b>	<b>4</b>
2.1 Permanent Magnet Scanners . . . . .	4
2.2 Magnetic Shimming . . . . .	4
2.3 Biot-Savart Law . . . . .	6
2.4 Pulse Sequences . . . . .	6
<b>3 Methodology</b>	<b>8</b>
3.1 Setup . . . . .	8
3.2 Local Shim Array . . . . .	9
3.3 Shimulation . . . . .	10
<b>4 Design</b>	<b>12</b>
4.1 Current Driver System . . . . .	12
4.2 Local Shim Array . . . . .	13
4.3 Coil Configuration Optimization . . . . .	15
4.4 Pulse Sequence . . . . .	21
4.5 Shimming Procedure . . . . .	24
<b>5 Experimentation</b>	<b>26</b>
5.1 Verification . . . . .	26
5.2 Results . . . . .	26
<b>6 Discussion</b>	<b>32</b>
6.1 Conclusion . . . . .	32
6.2 Future Work . . . . .	32

**Bibliography**



# List of Figures

- 1.1 Compares gradient echo scans at increasing time to echo (TE) values against a spin echo scan. Spin echos are generally resistant to  $B_0$  inhomogeneities. All four scans were performed in the Aspect II Wrist 1T MRI System. As TE increases, we notice distortions in the magnitude in the form of ringing and signal loss as well as a drift in phase. The artifacts due to  $B_0$  field inhomogeneity is especially noticeable in the upper left corner (circled in red). This disadvantage limits the different acquisition methods that can be implemented on a scanner with low field homogeneity such as echo planar imaging. . . . . 2
- 2.1 A demonstration of the difference in  $B_0$  direction between superconducting and permanent magnet scanners. Note that in the case of the superconducting scanner,  $B_0$  is along the length of the bore whereas in the case of permanent magnet scanners,  $B_0$  is orthogonal to the length of the bore. . . . . 5
- 3.1 The setup and initial design of our experiment. On the left is the Aspect Wrist II 1T MRI System. Connected inside of its bore is the scanner sleeve which contains the RF solenoid as well as the initial prototype of the local shim array. Many noise reduction implementations were added including the copper shielding over the magnet bore and RF-shielding over the twisted pairs connected to the power supplies. . . . . 8
- 3.2 A representation of how the magnetic field axes are oriented with relation to the scanner sleeve (left). The coronal and axial planes are orthogonal to the  $B_0$  and  $B_1$  axes respectively and the sagittal plane is orthogonal to the third axis. Our local  $B_0$  shim array is placed orthogonal to the  $B_0$  magnetic field on the coronal face of the RF solenoid which allows for maximum induced magnetic field while also minimizing coupling. . . . . 9
- 3.3 The simulations using the Biot-Savart toolbox [16]. The coil positions are shown in the bottom left and the fieldmap each coil produced is on the top. The fieldmaps of these six coils were fitted to the scanner fieldmap using (Eq. 3.1), producing the currents listed in the table. The image labeled “Difference” displays the fieldmap achieved when driving the solved currents into each coil. . . . 11

4.1	The boards that comprise the current driver system. From left to right: current driver board, fiber optic relay, Teensy microcontroller board [2]. The current driver board is one of two that is a part of our final system. The fiber optic connections allow for swift data transfer without loss over several meters, designed for high field scanning environments where the operating computer and scanner are in separate rooms. . . . .	13
4.2	The fully connected current amplifier system. This system is comprised of two amplifier boards mounted on a heat sink to dissipate the OPA549 amplifiers. Each board is connected to a 60A power supply via molex connectors and to the fiber optic relay via CAT6 cables. . . . .	14
4.3	Version 1 of the local shim array. Constructed on a polycarbonate sheet using copper tape soldered to twisted pairs. Connected to initial prototype power supplies as described in <b>Current Driver System</b> . Demonstrated mild coupling and significant noise contributions. . . . .	15
4.4	Version 2 of the local shim array. Constructed on kapton tape using 32 gauge copper magnet wire. Connected to improved current driver system as shown in Figure 4.2. Lessened the coupling problem associated with the wide copper tape. . . . .	16
4.5	The selected coils from each coil configuration optimization algorithm. Top left is the uniformly distributed coils over the surface area of the RF solenoid. Notice how mixed integer and joint sparsity seem to favor certain areas of the surface which seems to imply that there are more local inhomogeneities in these areas. Furthermore, unlike the non-greedy algorithms, matching pursuit seems to inundate the coronal face with coils. . . . .	20
4.6	Plots comparing the mean-squared-error (MSE) of the optimal coil configuration solutions in both the coronal and axial orientations. As expected, we can clearly rank the efficacy of each algorithm: MIO > JS > MP >> Uniform. Oddly enough, although MP seemed to fill the coronal faces with coils, it consistently underperforms in terms of MSE in that orientation. . . . .	21
4.7	Block sequence diagram of the slice-selective frequency calibration. This diagram shows $5 \times 512$ FID acquisitions of an excited slice with a dwell time of $40\mu s$ . This corresponds to a frequency bandwidth of 25kHz. The center frequency is determined to be that with largest signal amplitude. . . . .	22
4.8	Block sequence diagram of the fieldmap sequence. This diagram shows two $64 \times 64 \times 32$ (phase x frequency x slice) volumetric acquisitions with a delay in TE between the first 32 slices and the second 32 slices. It is important to note that the slice-selective loop is inside the phase-encoding loop which is how slice interleaving is implemented. With many slice, the effective TR can reduced by about an order of magnitude while maintaining high SNR. . . . .	23

5.1	Simulation verifications and SNR validations. To the left is a comparison of the simulations from Figure 3.3 and the magnetic fields in the $B_0$ direction generated by driving 1A through the coils shown in Figure 3.2. To the right is a comparison of SNR calculations with and without the shim coil array affixed onto the RF solenoid. The SNR was calculated by describing two circular regions of interest, one inside the phantom magnitude and another outside, and calculating the ratio of the standard deviations of each. The difference in center frequency between each fieldmap is due to frequency drift and not the shim coils. . . . .	27
5.2	The measured fieldmap of the coils for slice 16 of 32 (center slice of the imaging volume) connected to all 16 channels as well as the measured fieldmap of the linear gradient shims. Each coil was measured at 1A independently and each linear gradient shim was measured with a change in amplitude of 0.05 independently. .	28
5.3	Experimental results for slice 18 (+3mm from center) in the coronal orientation. The overall deviation without the shim array was calculated to be 3.1179 ppm. The overall deviation was calculated to be 1.0663 ppm. . . . .	29
5.4	Experimental results for slice 20 (+6mm from center) in the coronal orientation. The overall deviation without the shim array was calculated to be 2.1243 ppm. The overall deviation with the shim array was calculated to be 0.7727 ppm. . . .	30
5.5	Experimental results for slice 21 (+7.5mm from center) in the coronal orientation. The overall deviation without the shim array was calculated to be 1.9430 ppm. The overall deviation was calculated to be 0.9981 ppm. . . . .	31

## Acknowledgments

I wish to thank Professor Michael Lustig for the opportunity to work in his lab and invaluable guidance and support throughout the duration of this project.

A very special thank you to my collaborator Celine Veys. This project would not be possible without her contributions to and testing of all the complex hardware as well as the tireless hours spent on our joint collaborative efforts.

I would like to express appreciation to Dr. Jason Stockmann who provided us with assistance and resources for our final end-to-end hardware system. I am also grateful to Aspect Imaging for gifting our lab the Aspect Wrist II MRI system.

Thanks to Ekin Karasan and Victor Han, whose consultation regarding MR theory and hardware development at key milestones cannot be understated.

Finally, I would like to acknowledge my parents, Daniel Valentine and Maria Carmelita Calleja, as well as my siblings, Nikka and Miguel Calleja, for their unconditional support of my studies and wellbeing.

# Chapter 1

## Introduction

### 1.1 Motivation

In the realm of practical MRI machines, the source of the magnetic field can be divided roughly into two classes: superconducting and permanent magnets. Superconducting magnets are by far the most common in high-field, high-performance clinical use due to characteristics such as high field homogeneity, high spatial resolution, and increased T1 dispersion which allow them to acquire images of superior quality. Permanent magnets are generally categorized as low-to-mid field systems used in more routine scans and have the advantage of lower cost, improved accessibility, simpler siting requirements, increased portability, and less hardware. Dedicated permanent magnet MRI can be small, shielded, safe, and easy to site. However, the fact still remains that permanent magnets have inferior image quality when compared to their superconducting counterparts.

We specifically look at the poor field homogeneity of permanent magnets and how this affects scan quality (Figure 1.1). Field homogeneity is one of the most important characteristics of a scanner. It impacts the geometrical distortion (displacement of a voxel relative to its true position in space), the contrast of voxels (brightness of certain tissue relative to other tissues), and causes artifacts for many common pulse sequences.

Recent improvements in MR hardware, algorithms, and computation are being implemented to take advantage of the benefits of permanent magnets while minimizing the disadvantages. To address field inhomogeneity, there exist many conclusive improvements in the field of shim design. Towards this goal, we propose and upgrade for a wrist/animal 1T permanent-magnet system in the form of a simple localized  $B_0$  shim array. The intention of the localized shim array is to mitigate unwanted deviations in the permanent magnet scanner's magnetic field with minimal resources. This upgrade is constructed as an array of shim coils placed flush against the RF solenoid close to the subject. This allows the magnetic field generated by the coil to be more efficient in terms of power consumption.

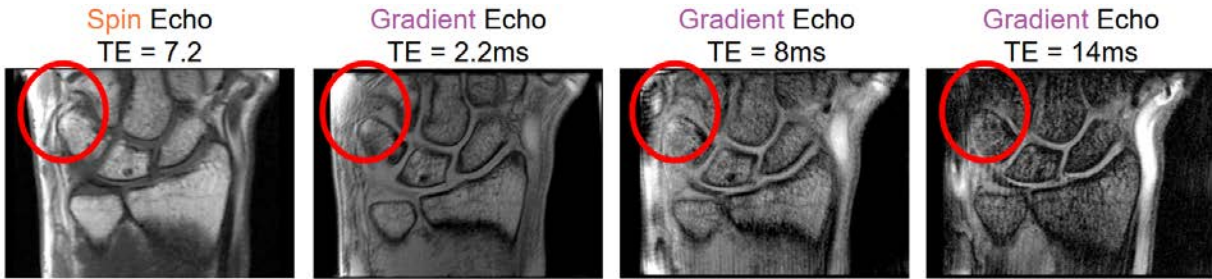


Figure 1.1: Compares gradient echo scans at increasing time to echo (TE) values against a spin echo scan. Spin echos are generally resistant to  $B_0$  inhomogeneities. All four scans were performed in the Aspect II Wrist 1T MRI System. As TE increases, we notice distortions in the magnitude in the form of ringing and signal loss as well as a drift in phase. The artifacts due to  $B_0$  field inhomogeneity is especially noticeable in the upper left corner (circled in red). This disadvantage limits the different acquisition methods that can be implemented on a scanner with low field homogeneity such as echo planar imaging.

## 1.2 Related Work

Prior work on shimming the magnetic field of magnetic resonance scanners have yielded impressive results.

Many shim designs implement passive shimming techniques involving the use of ferromagnetic materials placed in calculated locations. This has been shown to be effective in generating low-order homogeneous magnetic field harmonics while minimizing the amount of ferromagnetic material used [11]. Due to the physical properties of the shimming material, certain restrictions such as size and shape of the magnetic pieces as well as limitations on the location of placement and immobility must be met when designing a passive shim assembly [5]. In general, these physical constraints along with the magnetic shimming are taken into account in a series of equations involving magnetic coupling, Biot-Savart law, and spherical harmonic expansions and solved using various optimization methods (e.g. linear programming) to generate an optimal configuration for their placement [5, 17]. Recent developments in passive shim design have seen novel techniques implemented to increase the degrees of freedom with regards to many of the aforementioned restrictions [17] (e.g. size and shape of ferroschims). This specifically designs with relaxed constraints on the ferroschims geometries themselves affording greater flexibility in the implementation process. Other approaches look towards optimizing the design method to take advantage of the benefits of previous optimization algorithms [15] or refining the diameters of spherical volumes (DSV) of field inhomogeneities that the shim configuration solution is solving over [14].

The more common shim designs implement active shimming techniques which involve the use of current-carrying filaments surrounding the imaging volume. These shim coils

are again used to generate counter magnetic fields to fix inhomogeneities in the scanner fieldmap, but does so via current induced magnetic fields. While the general process of designing active shim coils is similar to that of designing passive ferroschims, the flexibility of the medium offers many freedoms for innovation. Active shims are commonly incorporated into the gradient coils themselves which are integral to the pulse sequences that drive MR imaging [23]. For the purposes of providing a shim over the entire DSV, many shim coils are designed to fit to the inner surface of the scanner in an arrangement that fits to the spherical harmonic expansions [6, 20]. For example, a shim coil can be shaped and placed in irregular patterns and the use of non-magnetic conductors such as copper does not restrict the placement of these coils to static positions around the DSV [22]. Developments in the orthogonal bases, such as the Fourier series, onto which the coil winding patterns are fitted also provide a new avenue of exploration [4].

This project examines a tangential category of local shim coils that are placed much closer to the subject. This has many advantages including increased  $B_0$ -to-current efficiency and the ability to shim highly localized inhomogeneities usually out of reach of standard shim coil configurations. One particular facet of local shim coils is the ability to perform low-current, dynamic shimming which decouples the coil design from the spherical harmonic expansion, reducing the complexity of fabrication by orders of magnitude [13]. The development of such coils has been shown to reduce  $B_0$  inhomogeneities with results comparable to that of spherical harmonic coils. Many works in this field have found success in increasing the proximity of the shim coils by integrating them into the RF coil arrays themselves [1, 7, 18]. This novel form of  $B_0$  shimming has many advantages, primarily due to the fact that the currents driving different applications can coexist independently within the same circuit with little to no electromagnetic interference between them [24, 12]. Such an implementation may be more feasible in the complex architecture of state-of-the-art MRI systems as it would require fewer modifications. Our project works towards this goal: to provide a simple but effective implementation of local shim coils.

# Chapter 2

## Background

### 2.1 Permanent Magnet Scanners

For the purposes of MRI, it is desirable for the scanning region to be within a highly homogeneous magnetic field (on the order of 1ppm variation). A homogeneous field can be defined as having constant, unidirectional magnitude [21]. As mentioned before, the fields of permanent magnets tend to have large inhomogeneities due to the nature of their construction. To achieve the levels of homogeneity, most scanner magnets are carefully designed to be within these specification. This is not an easy feat to achieve with permanent magnets as the magnet itself is very susceptible to the inevitable problems of fabrication errors and thermal contraction among other environmental factors.

The Halbach magnet array is a configuration of permanent magnets arranged such that for an infinitely long scanner, the magnets generate a strong and homogeneous, radially-oriented magnetic field inside the bore and zero field outside the bore [19]. This is a popular configuration for scanners with small diameter such as those used to scan specific parts of the body (e.g. head, hand) as it is able to achieve sufficient levels of field homogeneity necessary to acquire MR images.

The experiments in this project are performed using an Aspect Wrist II 1T MRI System which implements a Halbach magnet configuration to generate its magnetic field.

### 2.2 Magnetic Shimming

The magnetic field within the field-of-view of a scanner can be described as the summation of orthogonal functions. In many cases, the orthogonal functions come from the spherical



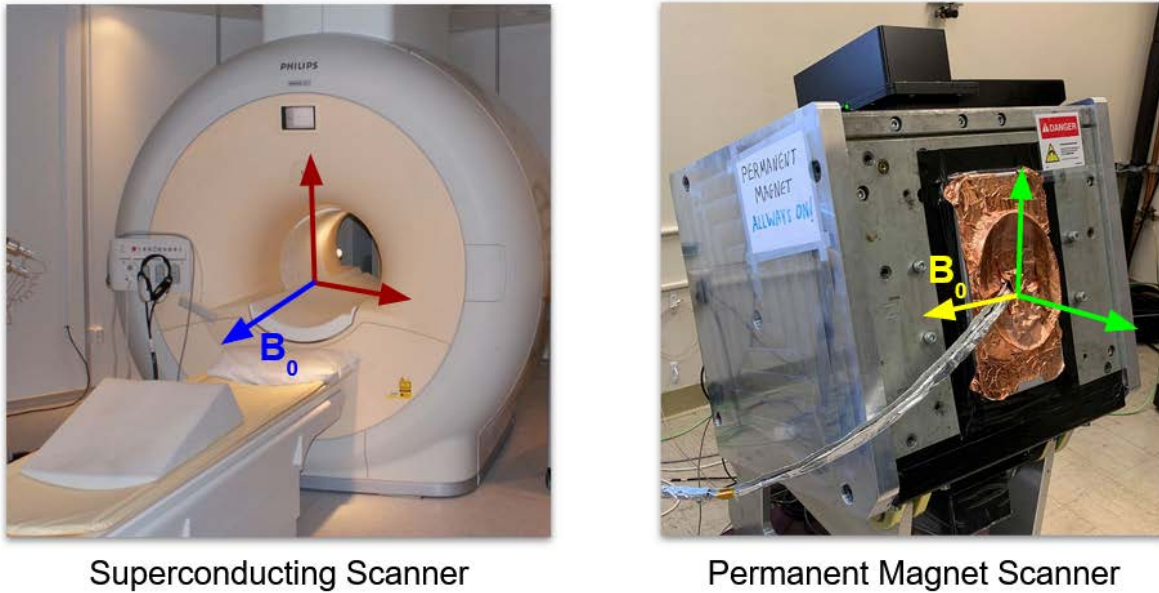


Figure 2.1: A demonstration of the difference in  $B_0$  direction between superconducting and permanent magnet scanners. Note that in the case of the superconducting scanner,  $B_0$  is along the length of the bore whereas in the case of permanent magnet scanners,  $B_0$  is orthogonal to the length of the bore.

harmonic expansion:

$$B_z(r, \theta, \phi) = \sum_{n=1}^{\infty} \sum_{m=0}^n r^n P_n^m(\cos \theta) \cdot [A_n^m \cos(m\phi) + B_n^m \sin(m\phi)] \quad (2.1)$$

where  $P_n^m(\cos \theta)$  is the Legendre polynomial of the first kind (with  $m$  and  $n$  integers and  $m \leq n$ ) and  $A_n^m$  and  $B_n^m$  are the undetermined coefficients [21].

For both superconducting and permanent magnet scanners, a process called shimming is used to remedy any deviations in the magnetic field introduced after the installation of the magnet system. This is performed by taking a measurement of the magnetic field within the scanner and generating a magnetic field to oppose any deviations. This opposing magnetic field can be calculated in a number of ways, usually done through a fitting to the spherical harmonic expansion (Eq. 2.1). By superimposing this generated field on top of the field produced by the scanner, many of the inhomogeneities can be eliminated.

Shimming methods can be divided into two categories, active and passive. Passive shimming involves the use of ferromagnetic material placed in or around the bore of the magnet. Typically, the ferromagnetic material is steel or iron. The main advantage of passive shim-

ming is that it requires no external power supply. Active shimming involves the use of resistive filaments (e.g. shim coils) arranged in such a way to generate a magnetic field within the magnet bore. These current carrying filaments are typically a non-magnetic material such as copper and can be placed in either a superconducting environment (cooled to the material's critical temperature) to reduce the power necessary to produce the driven current or at ambient temperature. Furthermore, due to the precise nature of the resulting counter magnetic field, active shimming generally requires a strong, highly stable power supply. The main advantage of active shimming is that the field the coils generate is a function of current which can be changed dynamically.

## 2.3 Biot-Savart Law

In active shimming, the magnetic field generated at a specific point by the shim coils can be calculated using Biot-Savart law [8]:

$$\vec{B}(\vec{p}) = \frac{\mu_0 I}{4\pi} \int \frac{\partial \vec{\ell} \times \hat{r}}{\|\vec{r}\|^2} \quad (2.2)$$

where  $\mu_0$  is the magnetic vacuum permeability constant,  $I$  is the current being driven through the conductor,  $\vec{\ell}$  is the length vector of the current carrying conductor, and  $\vec{r}$  is the vector from the length vector  $\partial \vec{\ell}$  to our point  $\vec{p}$ .

## 2.4 Pulse Sequences

A pulse sequence is an amalgamation of radiofrequency (RF) pulses, gradient pulses, and signal acquisition whose purpose is to manipulate the magnetization within a scanner in order to acquire data [3]. These pulse sequences are the heart of MR imaging and are found in virtually every MR application. There are five main magnetic-field manipulating components of a pulse sequence:

- **Radiofrequency (RF) Pulse** - a magnetic pulse in the transverse direction that excites hydrogen atoms to spin
- **Frequency-Encoding Gradient** - relates the Larmor frequency at which a hydrogen atom precesses to the spatial location along the gradient direction
- **Phase-Encoding Gradient** - relates the phase of the magnetization precession to the spatial location along the gradient direction
- **Slice-Selection Gradients** - modulates the RF pulse to relate the bandwidth of frequencies with a band of locations

- **Receiver Coil** - acquires the data generated by the above magnetic field manipulations by sampling the spatio-frequency ( $k$ -space) readouts of the excited voxels

Each event within a pulse sequence is defined by a number of fundamental parameters which govern the amplitude, frequency and shape of each pulse waveform including but not limited to:

- **Time to Echo (TE)** - time difference between the initial excitation by the RF pulse and the signal readout
- **Time to Repetition (TR)** - time difference between each successive excitation pulse
- **Dwell Time** - sampling period of receiver coil which determines the frequency bandwidth of the acquired image
- **Field-of-View (FOV)** - physical dimensions (in meters) of the acquired image
- **Number of Samples** - number of encodings in both the phase-encoding direction and the frequency-encoding direction
- **Pulse Type** - shape of the RF pulse which determines its power deposition, and frequency bandwidth

For the purposes of acquiring a 2D scan, most pulse sequences will follow a general set of instructions:

1. Generate an RF waveform modulated by the slice-selective gradients to excite a specific slice. This selects a 2D plane in the field-of-view to be scanned.
2. Generate a phase-encoding gradient pulse to select a line along the 2D plane.
3. Generate a frequency-encoding gradient pulse train to select points along the phase-encoding line and sample these points in  $k$ -space using the receiver coils.

# Chapter 3

## Methodology

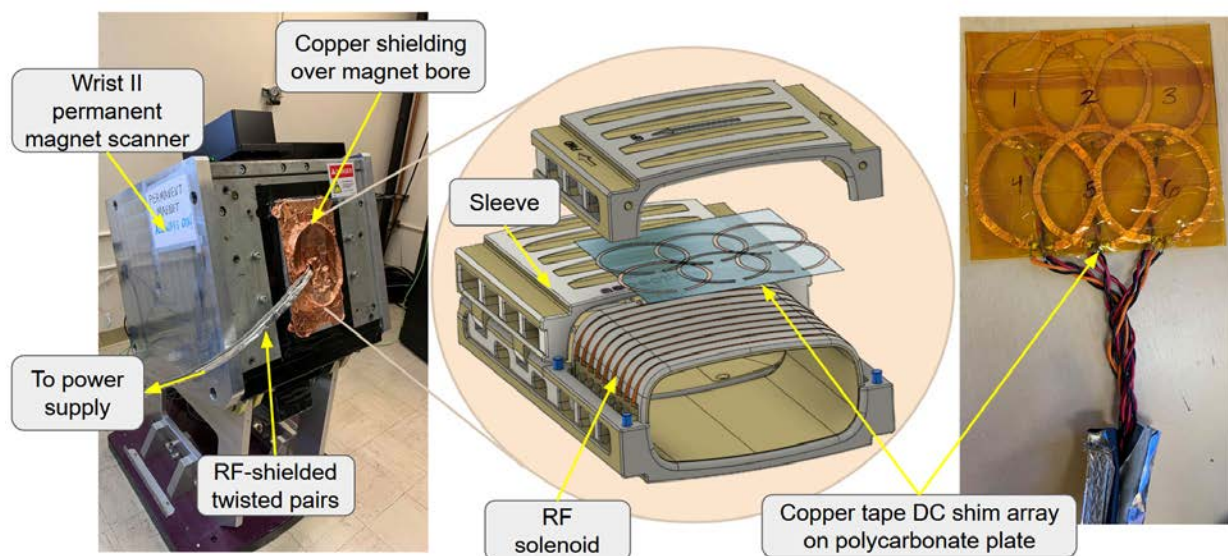


Figure 3.1: The setup and initial design of our experiment. On the left is the Aspect Wrist II 1T MRI System. Connected inside of its bore is the scanner sleeve which contains the RF solenoid as well as the initial prototype of the local shim array. Many noise reduction implementation were added including the copper shielding over the magnet bore and RF-shielding over the twisted pairs connected to the power supplies.

### 3.1 Setup

All studies and experiments throughout this research project were performed using an Aspect Wrist II 1T MRI System, using a wrist RF solenoid transmit-receive coil. The RF

solenoid covers a volume of  $\sim 500\text{cm}^3$  ( $10\text{cm} \times 10\text{cm} \times 5\text{cm}$ ) encased inside a plastic wrist-scanner sleeve.

It is important for the purposes of this project, that Aspect's wrist scanner system implements its RF transmit-receive hardware as a solenoid rather than a traditional coil. Due to the Halbach configuration of the scanner, this creates a  $B_1$  field in parallel with the length of the subject. Furthermore, this creates an ideal framework to create a local resistive shim array.

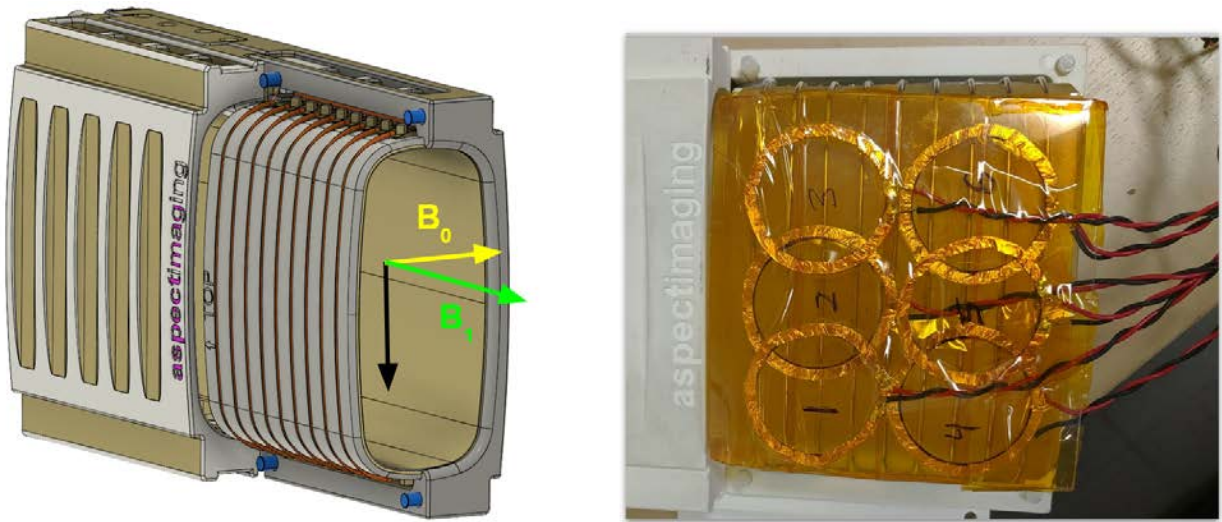


Figure 3.2: A representation of how the magnetic field axes are oriented with relation to the scanner sleeve (left). The coronal and axial planes are orthogonal to the  $B_0$  and  $B_1$  axes respectively and the sagittal plane is orthogonal to the third axis. Our local  $B_0$  shim array is placed orthogonal to the  $B_0$  magnetic field on the coronal face of the RF solenoid which allows for maximum induced magnetic field while also minimizing coupling.

## 3.2 Local Shim Array

The RF solenoid generates a  $B_1$  field in parallel with the length of the subject. The scanner generates a  $B_0$  field perpendicular with the length of the subject. Due to these two facts, we theorized the construction of a shim array located proximal to the region-of-interest (ROI). As described by (Eq. 2.2), the strength of a magnetic field at a point,  $\vec{p}$ , generated by a current-carrying filament,  $\partial\vec{\ell}$ , is inversely proportional to the square of the distance between  $\vec{p}$  and  $\partial\vec{\ell}$ . This means that the closer our shim array is to the ROI, the less current is necessary to achieve the desired fieldmap. Overall this affords lower power consumption, cheaper hardware, and more efficient usage of space.

On top of the above advantages, the RF solenoid’s surface area ( $\sim 300\text{cm}^2$ ) is a proper space onto which we affix the shim coil array onto. We design a shim coil array onto the faces of the solenoid that are orthogonal to the  $B_0$  field. Due to hardware and space constraints, we are softly limited to 16-channels and therefore we constructed eight coils on either side of the solenoid’s surface.

### 3.3 Shimulation

Every shim begins with characterizing the inhomogeneities that exist within the field-of-view (FOV) of the scanner. To acquire this data, we used a copper sulfate ( $\text{CuSO}_4$ ) doped bottle phantom as our subject. We acquired fieldmap data through a two-scan gradient echo sequence with a delay in acquisition.

To get an idea of what our end results should look like, we wrote a Biot-Savart simulation to estimate the  $B_0$  fieldmap contributions within the field-of-view (FOV) of the RF solenoid for an arbitrary number and size of shim coils. For a target slice, we displayed the contributions of six circular shim coils of uniform radius to cover as much area of the RF solenoid’s FOV. The code was implemented in MATLAB.

Given each coil’s  $B_0$  field contribution as well as the target fieldmap, a least-square shimming procedure was used to determine the optimal shim-currents. In the following minimization problem, we look at a target slice at index  $i$ , each column of  $A_i$  represents the  $B_0$  field contribution of a coil in the shim array and  $b_i$  represents the target fieldmap.

$$\begin{aligned} \min_x \quad & \|A_i x + b_i\|_2 + \psi \|(A_{i-1} + A_{i+1})x + (b_{i-1} + b_{i+1})\|_2 + \lambda \|x\|_1 \\ \text{s.t.} \quad & |x| < 2 \end{aligned} \tag{3.1}$$

In order to ensure that the fieldmap gradient is smooth along the slice orientation, we add the  $i - 1$  and  $i + 1$  terms scaled by the hyperparameter  $\psi$  to our optimization. Furthermore, to minimize the total current needed by our system, we include an  $L_1$  regularization as well as hard constraints.

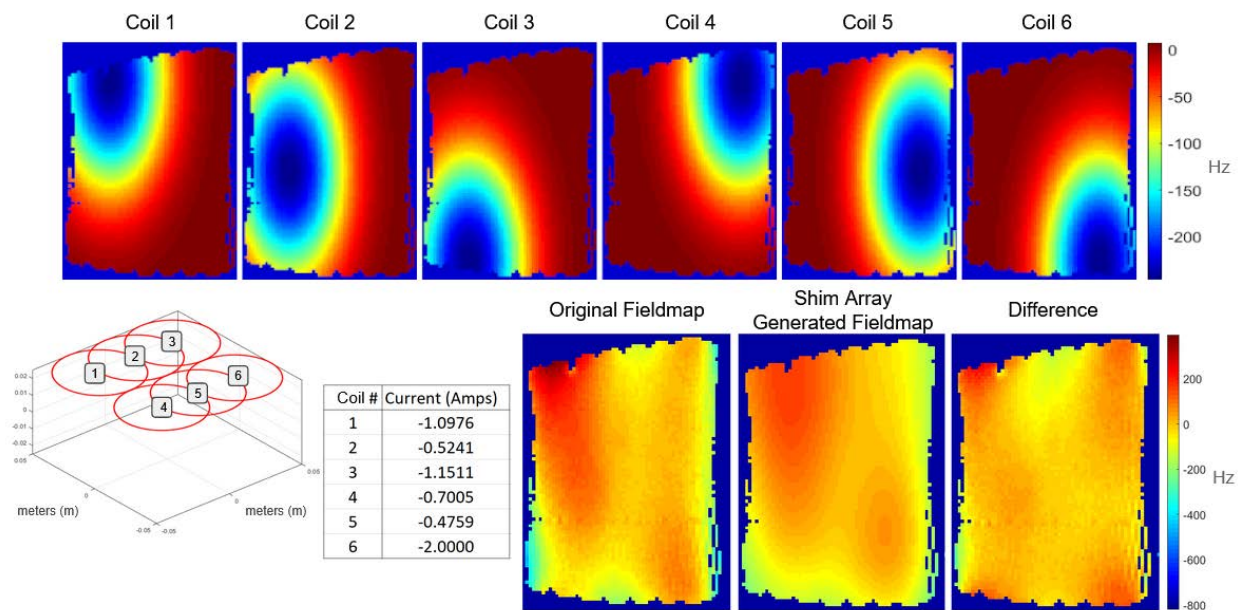


Figure 3.3: The simulations using the Biot-Savart toolbox [16]. The coil positions are shown in the bottom left and the fieldmap each coil produced is on the top. The fieldmaps of these six coils were fitted to the scanner fieldmap using (Eq. 3.1), producing the currents listed in the table. The image labeled “Difference” displays the fieldmap achieved when driving the solved currents into each coil.

# Chapter 4

## Design

### 4.1 Current Driver System

Throughout the duration of this project, electrical noise has been a constant obstacle to overcome due to the many interconnected components. The current drivers which supply the current through each shim coil, arguably the most important electrical source, needs to be highly stable and resistant to noise.

Our initial prototype of this system included the use of five, single-channel and three, two-channel power supplies to drive our Version 1 implementation of the shim array with twelve coils. This introduced not only many sources of noise, but also limited our current value precision to only two decimal places. Furthermore, the current values had to be set at shim-time by hand.

Thankfully, a team at Massachusetts General Hospital generously gifted us a current driver system. This consisted of three components:

- **Teensy Microcontroller** - Programmatically sends calibration and read/write commands for each connected current channel to each connected current driver board.
- **Fiber Optic Relay** - Acts as a relay between the microcontroller and up to eight current driver boards.
- **Current Driver Board(s)** - Supplies eight independent channels with up to 8A of feedback controlled, DC current designed specifically for matrix shim coil arrays. Robust against both general noise and disturbances caused by gradient switching in an MRI scanner environment.



This current driver system not only significantly improved our setup, but also makes dynamic shimming a viable next-step towards which this project can be developed.

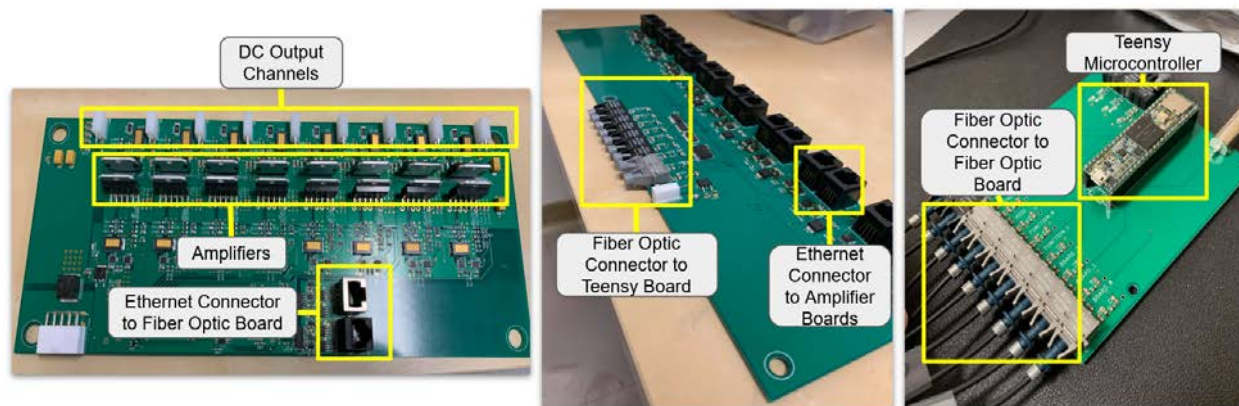


Figure 4.1: The boards that comprise the current driver system. From left to right: current driver board, fiber optic relay, Teensy microcontroller board [2]. The current driver board is one of two that is a part of our final system. The fiber optic connections allow for swift data transfer without loss over several meters, designed for high field scanning environments where the operating computer and scanner are in separate rooms.

## 4.2 Local Shim Array

Due to the characteristics of the permanent magnet scanner in addition to the RF solenoid mentioned previously, there were constraints on the physical implementation of our shim array:

1. **Thickness** - The space between the RF solenoid and the sleeve as well as between the sleeve and the wall of the magnet bore is limited.
2. **Resistance** - The shim coil array would be flush with the RF solenoid which is thermally sensitive. Furthermore, the solenoid is only  $\sim 1\text{mm}$  thick and any heat generated by the shim coils would ultimately be transferred to the subject.
3. **Magnetism** - As with most hardware implemented for MRI, the metallic elements must be non-magnetic (e.g. brass, aluminum, copper) as it will be directly within a 1T field.
4. **Coupling** - Due to the proximity of the shim coils and the RF solenoid, the likeliness that the conductive elements between the two could couple and cause interference in their respective functions was high.

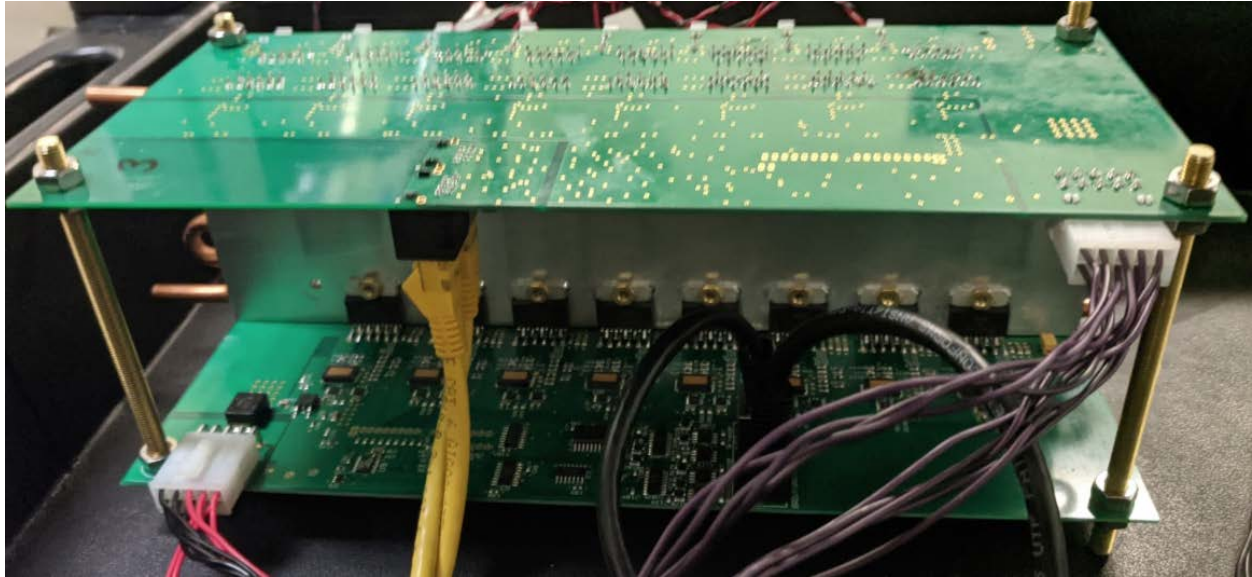


Figure 4.2: The fully connected current amplifier system. This system is comprised of two amplifier boards mounted on a heat sink to dissipate the OPA549 amplifiers. Each board is connected to a 60A power supply via molex connectors and to the fiber optic relay via CAT6 cables.

### Version 1

Our initial prototype was implemented using 2mm wide copper tape on top of a 0.5mm polycarbonate sheet. This design neatly fit into the dimensions of the scanning sleeve and fit all the criterion for low resistance and non-magnetism. Each copper tape coil measured to be  $\sim 0.8\Omega$ . The use of copper tape in this iteration was due to its adhesiveness which lent itself well to ease of construction. Twelve coils were constructed, six on either coronal face of the RF solenoid. Each coil was evenly spaced with a radius of  $\sim 2.5\text{cm}$  to maximize coverage of the FOV. The flaw of this design was the width of the copper tape, which caused measurable coupling with the RF solenoid.

### Version 2

The second iteration was made to explore the potential advantages of shim coils on the edges of our field of view. This was accomplished by adding four additional coils to the short face of the RF solenoid orthogonal to both  $B_0$  and  $B_1$ . In order to accommodate these coils and minimize the coupling problem from Version 1, the entire coil array was constructed on a sheet of kapton tape using 32 gauge magnet wire. The coils were of the same dimensions and location as in Version 1. 16 coils were constructed, six on either coronal face of the RF solenoid and two on either axial face. The entire kapton sheet was wrapped around the RF

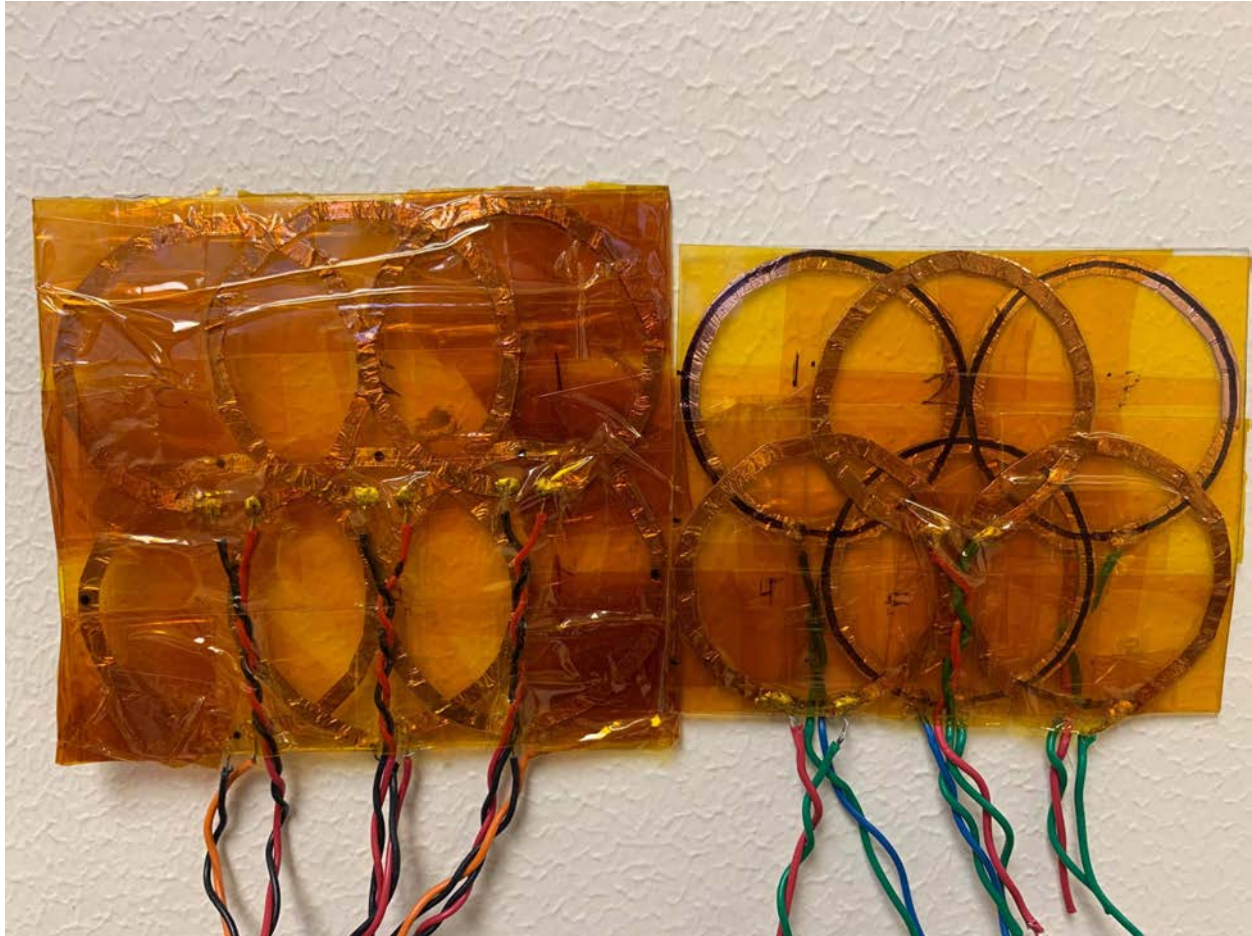


Figure 4.3: Version 1 of the local shim array. Constructed on a polycarbonate sheet using copper tape soldered to twisted pairs. Connected to initial prototype power supplies as described in **Current Driver System**. Demonstrated mild coupling and significant noise contributions.

solenoid. We found new coupling problems, this time due to the proximity of the new coils to the resonance-tuning capacitors on the axial face of the RF solenoid. This was fixed by adding magnet foam spacers between the coupling elements.

### 4.3 Coil Configuration Optimization

A small digression from the iterative design process was taken to investigate design optimization. The design versions talked about previously implemented uniformly spaced, circular shim coils with identical radii primarily because they are easy to simulate and construct. However, this is in no way optimized for the magnetic field volume which we are attempting



Figure 4.4: Version 2 of the local shim array. Constructed on kapton tape using 32 gauge copper magnet wire. Connected to improved current driver system as shown in Figure 4.2. Lessened the coupling problem associated with the wide copper tape.

to shim. We performed a few algorithms built on top of the original minimization problem described in (Eq. 3.1). Broadly speaking, these algorithms search a finite set of potential shim configuration and chooses those coils whose current contributions in amperes are most significant. The finite set of shim configurations we created for this problem was 138 circular coils of varying radii ranging from 2cm to 5cm spread out over the face of the RF solenoid. Each of the 138 coils were simulated over a meshgrid of size  $128 \times 70 \times 64$  over an FOV of  $10\text{cm} \times 10\text{cm} \times 5\text{cm}$ . For all of the algorithms we implemented, the minimization problem was solved over all individual slices within the volume of the FOV. This requires slightly

new notation as the vector of currents we solve for in (Eq. 3.1) is now a matrix where the value  $x_{c,n}$  represents the current for coil  $c$  at slice  $n$ .

## Joint Sparsity Optimization

One algorithm we used built upon (Eq. 3.1) and added a regularization term on top of it:

$$\begin{aligned} \min_x \quad & \sum_{n=1}^N [ \|A_n x_n + b_n\|_2 + \psi \| (A_{n-1} + A_{n+1}) x_n + (b_{n-1} + b_{n+1}) \|_2 ] + \lambda \sum_{n=1}^N \|x_n\|_1 \\ \text{s.t.} \quad & |x| < 2 \end{aligned} \quad (4.1)$$

We call the term multiplied by the hyperparameter  $\lambda$  the “joint-sparsity” term as it links together the solution for the current in coil  $c$  across all slices within the volume. Intuitively, this regularization term enforces an  $L_1$ -regularization on each coil’s current contribution which forces much of the solution to zero. It is important that many of the solved currents are zero as this will make the significant coils more obvious. The number of “significant” coils is defined as the coils whose average current across all slices is greater than some nominal threshold. We want the optimization itself to “find” the 16 optimal coils and so we iterate over the hyperparameter  $\lambda$  whose value is inversely proportional to the number of significant coils. Another method of choosing the optimal coils would be to sort the current contributions of each coil in descending order and selecting the top 16 coils.

---

### Algorithm 1: Joint Sparsity Optimization

---

**input:**  $\mathbf{A}$  -  $O \times C \times N$  matrix of fieldmap contributions from  $C$  coils and gradients with  $O$  observation points for  $N$  slices  
 $\mathbf{b}$  -  $O \times N$  vector containing  $O$  observations for  $N$  slices of the target fieldmap

**output:** The 16 coils with the most significant current contribution

```

1  $\lambda = 1$ 
2 while numSigCoils != 16 do
3   Use CVX [9, 10] to solve (Eq. 4.1)
4   numSigCoils = count(coils with significant current contribution)
5   if numSigCoils > 16 then
6     | increase  $\lambda$ 
7   else if numSigCoils < 16 then
8     | decrease  $\lambda$ 
9   else
10  | break
11 end

```

---

## Mixed Integer Optimization

We implemented an optimization procedure from a class of optimization programs called integer programs. This subspace of optimization programs is useful in formulating non-continuous objective functions and constraints. This is relevant to our coil configuration optimization as we are searching for an exactly sized optimal set of coils within a large superset of coils.

Unfortunately, integer constraints are non-convex, more difficult to solve, and theoretically intractable. Due to the immense scale of the search space, we chose to first reduce our problem from the original 138 coils. This was done through a iterative method of solving the simple convex problem described in (Eq. 3.1) over all slices. The solution was sorted by significant current contributions, defined as the norm of the solutions for a given coil,  $\|x_{c,:}\|_1$ . This process was iterated over from 138 down to 32 in arbitrary step sizes.

The minimization problem is extended from (Eq. 3.1):

$$\begin{aligned}
 \min_x \quad & \sum_{n=1}^N \|A_n x_n + b_n\|_2 + \lambda \|x_n\|_1 + \psi \|(A_n + A_{n+1}) + (b_{n-1} + b_{n+1})\|_2 \\
 \text{subject to} \quad & |x| \leq 2 * p, \\
 & \sum p = 16
 \end{aligned} \tag{4.2}$$

where  $p$  is a binary vector which constrains the total number of coils in the solution  $x$  to be 16.

---

**Algorithm 2:** Iterative sort reduction and mixed integer optimization

---

**input:**  $\mathbf{A}$  -  $O \times C \times N$  matrix of fieldmap contributions from  $C$  coils and gradients with  $O$  observation points for  $N$  slices  
 $\mathbf{b}$  -  $O \times N$  vector containing  $O$  observations for  $N$  slices of the target fieldmap

**output:** The 16 coils with the most significant current contribution

```

1 selectedCoils = [1:138]
2 currentNumCoils = 138
3 reduceCoilNumBy = 5
4 while currentNumCoils > 32 do
5   Use CVX [9, 10] to solve the problem 3.1;
6   Sort norm of solution x from greatest to least, and select top
   currentNumCoils - reduceCoilNumBy
7   currentNumCoils -= reduceCoilNumBy
8 end
9 Use CVX [9, 10] to solve the problem 4.2
10 selectedCoils = selectedCoils(p==1)
```

---

## Matching Pursuit

Matching pursuit (MP) is a common greedy algorithm for selecting basis functions to fit to some signal. These basis functions are commonly referred to as a dictionary. We generalized this to our coil configuration optimization problem by assigning the coil fieldmaps as the dictionary and the scanner fieldmap as the signal to which we wanted to fit. The matching pursuit algorithm first initializes the dictionary, the target function, and a residual. This initial residual tends to be the target function itself, however because our problem always includes the linear gradient shims as a part of the solution, our residual initializes to the difference between the target function and the best fit gradient shim. From there, we iterate and find the coil that fits to the residual and add that to our solution, calculating a new residual as the difference between the target function and our solution's best fit. This iteration continues until we have 16 coils.

This greedy algorithm acted as a good reference point for how well both **Mixed Integer** and **Joint Sparsity** performed.

**Algorithm 3:** Matching pursuit

---

**input:**  $\mathbf{A}$  -  $O \cdot N \times C$  matrix of fieldmap contributions from  $C$  coils and gradients with  $O$  observation points for  $N$  slices  
 $\mathbf{b}$  -  $O \cdot N$  vector containing  $O$  observations for  $N$  slices of the target fieldmap

**output:** The 16 coils with the most significant current contribution

- 1 selected = [gradientX, gradientY, gradientZ]
- 2 selectedFieldmaps =  $\mathbf{A}(:, \text{selected})$
- 3 optVals = solution to (Eq. 3.1) for selectedFieldmaps
- 4 residual =  $\mathbf{b} - \text{selectedFieldmaps} \cdot \text{optVals}$
- 5 **for**  $i = 1$  to 16 **do**
- 6     nextSelected =  $\text{argmax}(\mathbf{A} \cdot \text{residual})$
- 7     append nextSelected to selected
- 8     selectedFieldmaps =  $\mathbf{A}(:, \text{selected})$
- 9     optVals = solution to (Eq. 3.1) for selectedFieldmaps
- 10    residual =  $\mathbf{b} - \text{selectedFieldmaps} \cdot \text{optVals}$
- 11 **end**

---

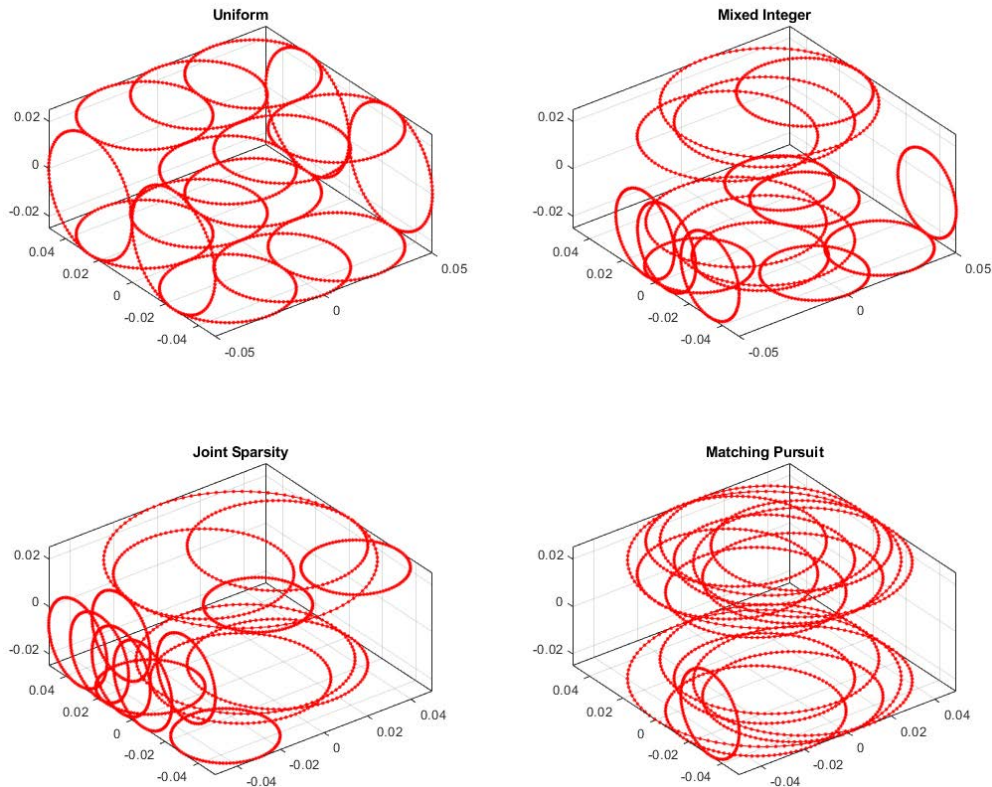


Figure 4.5: The selected coils from each coil configuration optimization algorithm. Top left is the uniformly distributed coils over the surface area of the RF solenoid. Notice how mixed integer and joint sparsity seem to favor certain areas of the surface which seems to imply that there are more local inhomogeneities in these areas. Furthermore, unlike the non-greedy algorithms, matching pursuit seems to inundate the coronal face with coils.



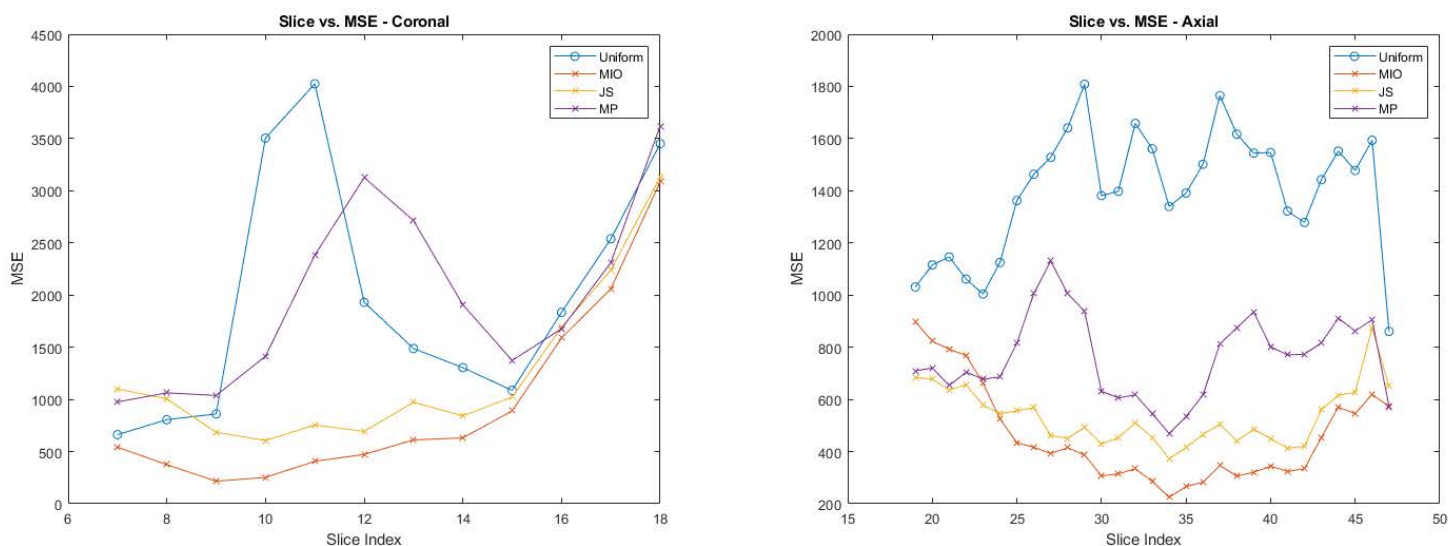


Figure 4.6: Plots comparing the mean-squared-error (MSE) of the optimal coil configuration solutions in both the coronal and axial orientations. As expected, we can clearly rank the efficacy of each algorithm:  $MIO > JS > MP \gg$  Uniform. Oddly enough, although MP seemed to fill the coronal faces with coils, it consistently underperforms in terms of MSE in that orientation.

## 4.4 Pulse Sequence

Running a targeted shim required the implementation of two different pulse sequences: Slice Selective Frequency Calibration and a Two-Scan TE-Delayed Gradient Echo Fieldmap.

### Frequency Calibration

Frequency Calibration is used to set the center frequency of all other scanning procedures which is important for generating the RF pulse. This center frequency tends to be around the Larmor frequency (e.g. 42.58 MHz at 1T) which is the resonant frequency of protons, but changes depending on the subject material, the  $B_0$  field, and the scanner type. For permanent magnet scanners specifically, frequency drift is a major problem. The Aspect II Wrist 1T MRI System reports a frequency drift of about 1Hz per second. For pulse sequences that have a minimum scanning time of 30 seconds, this is a significant problem.

The Slice Selective Frequency Calibration sequence is implemented to determine what the optimal center frequency is for a target slice. This is done by exciting the target slice with an RF pulse modulated by the slice-selective gradient and then acquiring multiple free-induction decay (FID) signals at a fast sampling period (e.g. Dwell Time < 50ms). The

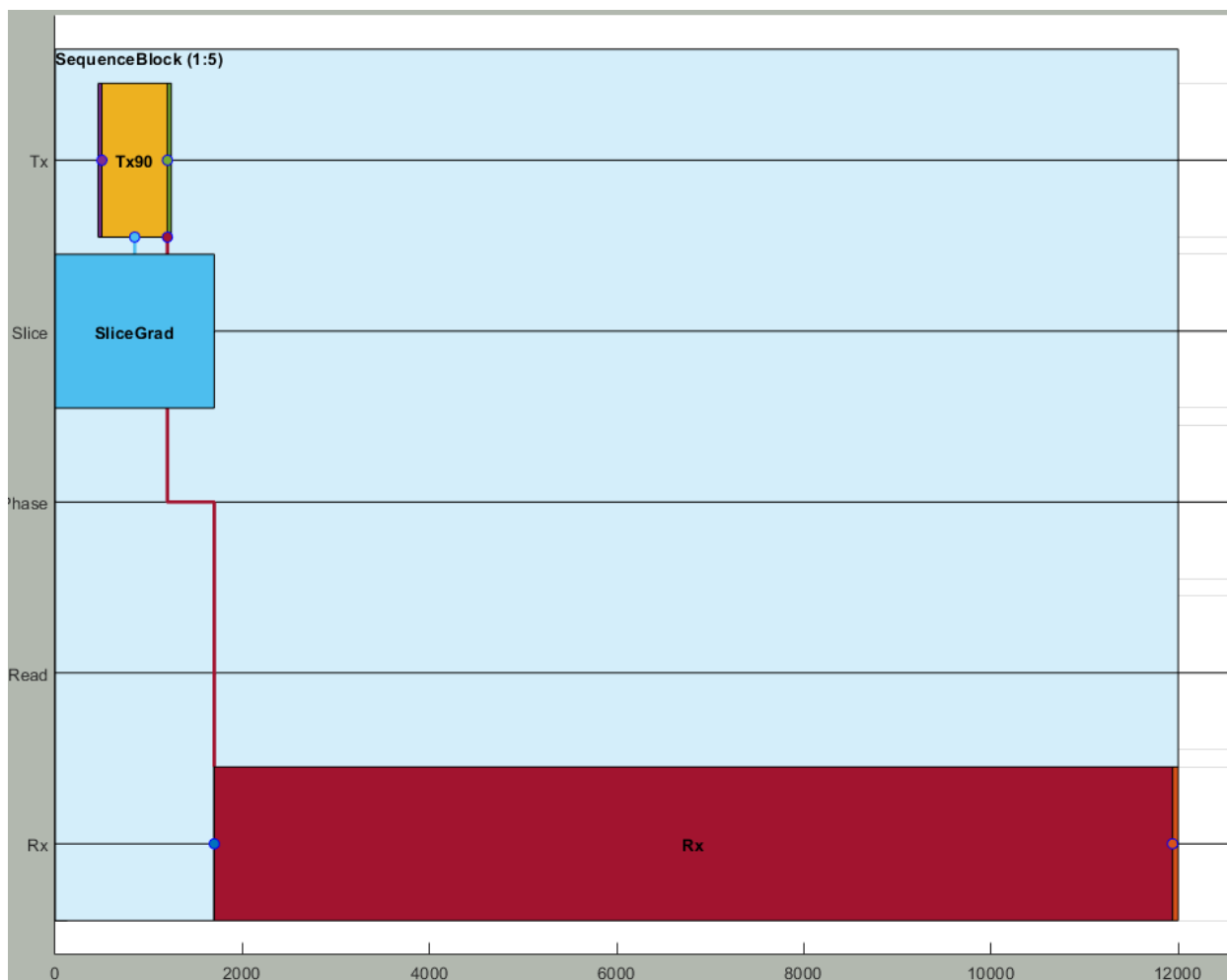


Figure 4.7: Block sequence diagram of the slice-selective frequency calibration. This diagram shows  $5 \times 512$  FID acquisitions of an excited slice with a dwell time of  $40\mu\text{s}$ . This corresponds to a frequency bandwidth of 25kHz. The center frequency is determined to be that with largest signal amplitude.

inverse Fourier transform of these FID signals should reveal a peak frequency at which the excited protons are precessing. By averaging the iFFT of the FID signals, we can get a good estimate of what the nominal center frequency should be for a given slice.

## Fieldmap Sequence

Although there are a handful of ways to calculate the fieldmap of a DSV, the Two-Scan TE-Delayed Gradient Echo sequence is fast, lightweight, and easy to implement. The basic gradient echo sequence is as follows:

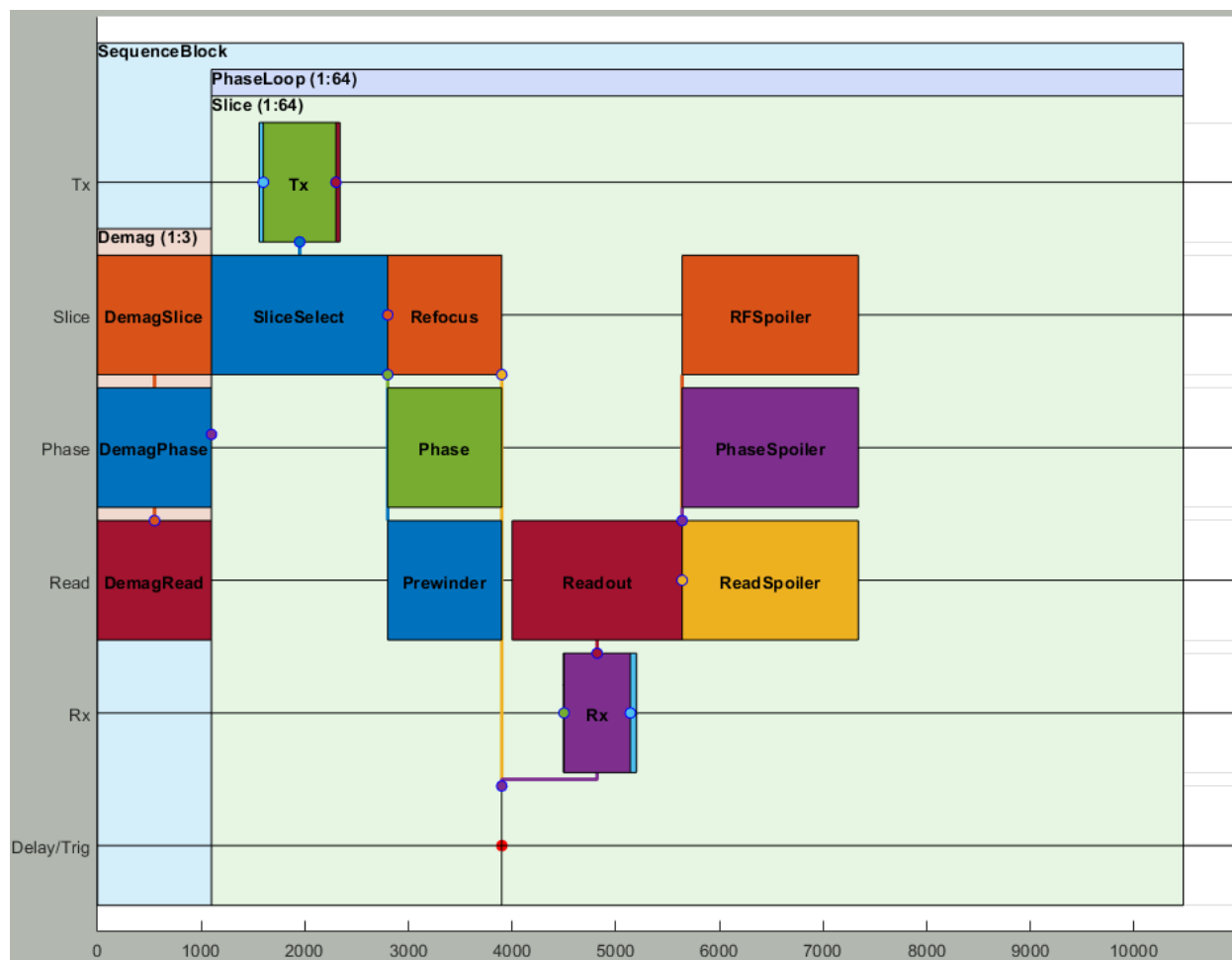


Figure 4.8: Block sequence diagram of the fieldmap sequence. This diagram shows two  $64 \times 64 \times 32$  (phase x frequency x slice) volumetric acquisitions with a delay in TE between the first 32 slices and the second 32 slices. It is important to note that the slice-selective loop is inside the phase-encoding loop which is how slice interleaving is implemented. With many slice, the effective TR can be reduced by about an order of magnitude while maintaining high SNR.

1. Excite a target slice (Flip Angle  $< 90^\circ$ ) using a slice-selective gradient modulated RF pulse
2. The frequency-encoding gradient applies a negative gradient called a “dephasing gradient” which modifies the spin phase in a spatially dependent manner
3. The frequency-encoding gradient applies a positive gradient of equal magnitude to compensate for the effect of the dephasing gradient

4. When the area of the positive gradient equals that of the dephasing gradient, the phases of the spins will realign and create an “echo”

The gradient echo sequence will acquire FIDs for an entire DSV which can be used to generate a 3D image. However, in order to calculate a fieldmap using gradient echo sequences, another image must be acquired at a delayed time-to-echo (TE). This refers to delaying the readout of the pulse sequence by some small number of milliseconds,  $\Delta\text{TE}$ . With a difference in TE, the two images will have slightly different phases related to the overall  $B_0$  field. For two images,  $\text{TE}_1$  and  $\text{TE}_2$ , and conjugation operator,  $*$ , the fieldmap can be calculated as:

$$\frac{\angle(\text{TE}_1^* \cdot \text{TE}_2)}{\Delta\text{TE}} \quad (4.3)$$

Certain optimizations were taken to speed up this sequence. To speed up 3D scans we implemented slice interleaving, a technique in which every other slice is excited at a much shorter repetition time (TR) in order to take advantage of the relaxation time (T2) of excited protons. We also implemented spoiler gradients which are large gradient pulses at the end of a scanline acquisition to “reset” the magnetization within the DSV. This allows the TR to be even shorter as we no longer have to wait the full relaxation time before exciting another slice.

## 4.5 Shimming Procedure

The process we implement for our shim array system is a targeted shim. A targeted shim corrects the field inhomogeneities for a target slice. In order to accomplish this we performed the following steps:

1. **Characterization** - The fieldmap for each coil in the shim array and linear gradient shim must be characterized to determine the induced magnetic field. First a fieldmap with no induced magnetic field is measured, followed by the fieldmaps of all 19 components of our minimization problem (16 coils + 3 gradients). Each coil is measured at 1A and each linear gradient shim is measured with a 0.05 change in amplitude. This step can be precomputed a single time for a given shim array - phantom pair and reused for future shims.
2. **Minimization Solution** - Each of the measured fieldmaps are masked and reshaped into vectors and concatenated into a single matrix. We then solve (Eq. 3.1) for the target slice.

3. **Solution Input** - The solved current for each coil is sent to the current driver board through the Teensy microcontroller via MATLAB serial connection. The solved amplitude for each linear gradient shim is sent to the scanner system through SQL.
4. **Slice-Selective Frequency Calibration** - To account for measurement errors regarding the center frequency from the **Characterization** step, the slice-selective frequency calibration sequence is run. The calculated frequency shift is sent to the scanner system through SQL.

# Chapter 5

## Experimentation

### 5.1 Verification

In order to ensure that our coils agreed with our simulations from Figure 3.3, we measured the fieldmaps of the copper tape shim coil array. Once we observed that the resulting fieldmaps showed satisfactory correspondence with the simulations, we also took SNR measurements with and without the shim coil array to ensure that there was not significant coupling between the shim array and the RF solenoid. This is displayed in Figure 5.1. Once our simulations were verified we increased the number of channels in the shim array from 6 to 16. The resulting fieldmaps displayed in Figure 5.2 matches closely to the locality of each coil. It is important to note that due to the frequency drift of the Aspect Wrist II 1T MRI System, the center frequency of each coil fieldmap is not accurate. Furthermore, each measurement of the shim coil fieldmap carries unavoidable noise which manifests itself in the minimization solution.

### 5.2 Results

To demonstrate the efficacy of our targeted shim implementation, we display side-by-side images of the original fieldmap, the theoretical best simulated fieldmap achievable with our 16 channel shim array plus linear gradient shims, and the observed fieldmap with the minimization solution input into all 16 channels and linear gradient shims. This is displayed in the coronal orientation for slices 18, 20, and 21 of 32 in Figures 5.3, 5.4, and 5.5 respectively. For each targeted shim instance, a slice-selective frequency calibration was performed in order to mitigate the effects of center frequency offsets in the measurement of the coil fieldmaps. While this slice-selective frequency calibration performed its job relatively well, there were still some disagreements with the theoretical best achievable shim. Below the fieldmap images are vertical and horizontal cross-sectional plots to show how well the observed shim corresponds with the theoretical best as well as a histogram to give an idea of

the distribution of deviations in the magnetic field. We calculate the deviation in ppm for each of the instances through the equation:

$$\text{ppm} = \frac{\text{std in Hz} \cdot 10^6}{42.58\text{MHz}} \quad (5.1)$$

For these three instances, we find that the overall inhomogeneity measured in the magnetic field after applying the minimization solution to our local shim array is close to the 1 ppm field variation at 1T reportedly required for some MRI sequences [20].

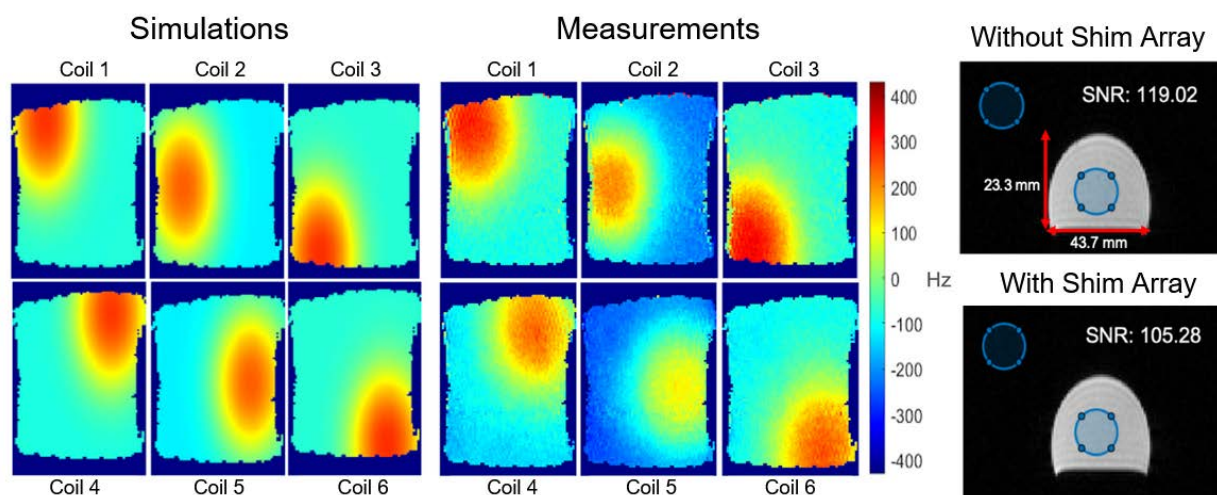


Figure 5.1: Simulation verifications and SNR validations. To the left is a comparison of the simulations from Figure 3.3 and the magnetic fields in the  $B_0$  direction generated by driving 1A through the coils shown in Figure 3.2. To the right is a comparison of SNR calculations with and without the shim coil array affixed onto the RF solenoid. The SNR was calculated by describing two circular regions of interest, one inside the phantom magnitude and another outside, and calculating the ratio of the standard deviations of each. The difference in center frequency between each fieldmap is due to frequency drift and not the shim coils.

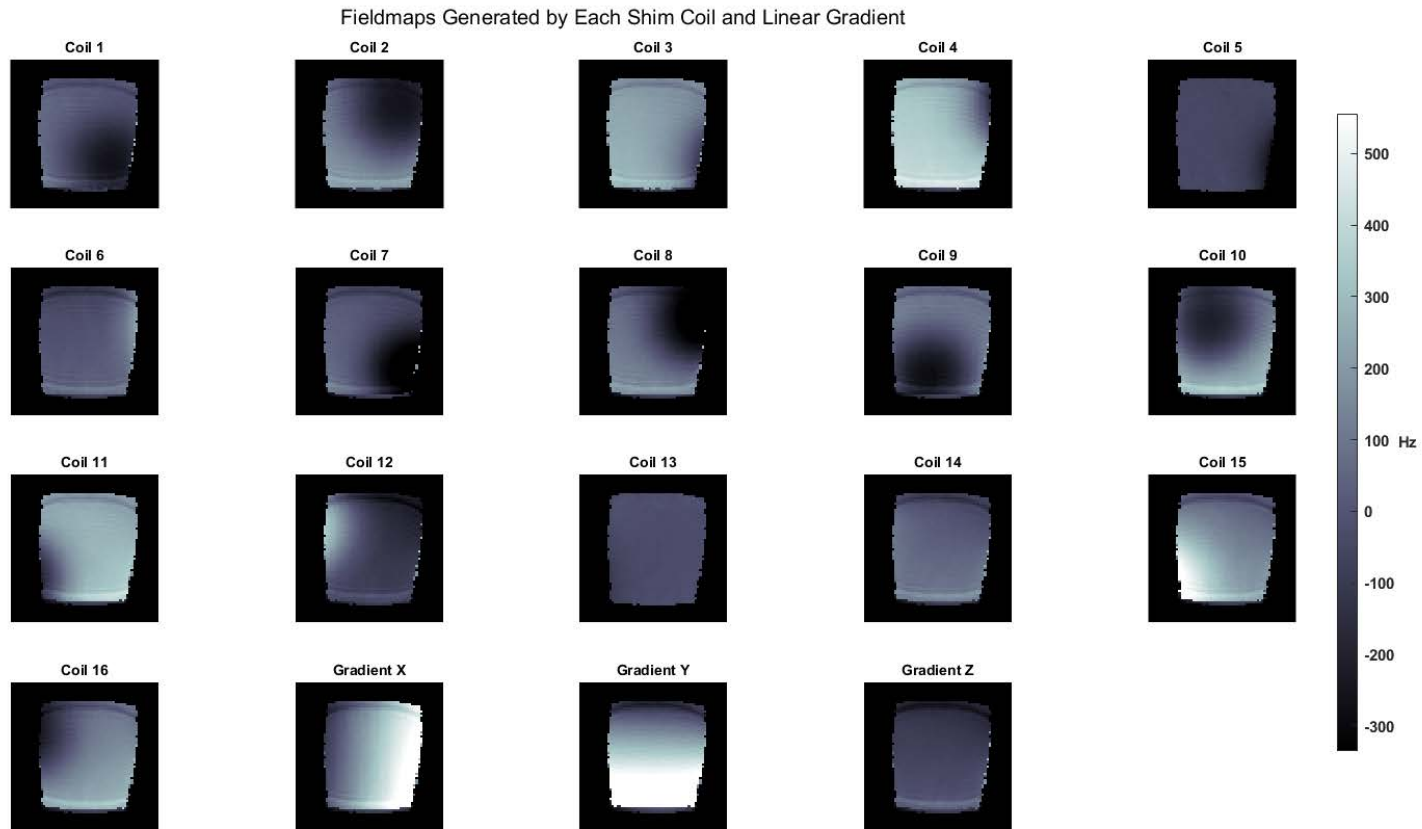


Figure 5.2: The measured fieldmap of the coils for slice 16 of 32 (center slice of the imaging volume) connected to all 16 channels as well as the measured fieldmap of the linear gradient shims. Each coil was measured at 1A independently and each linear gradient shim was measured with a change in amplitude of 0.05 independently.



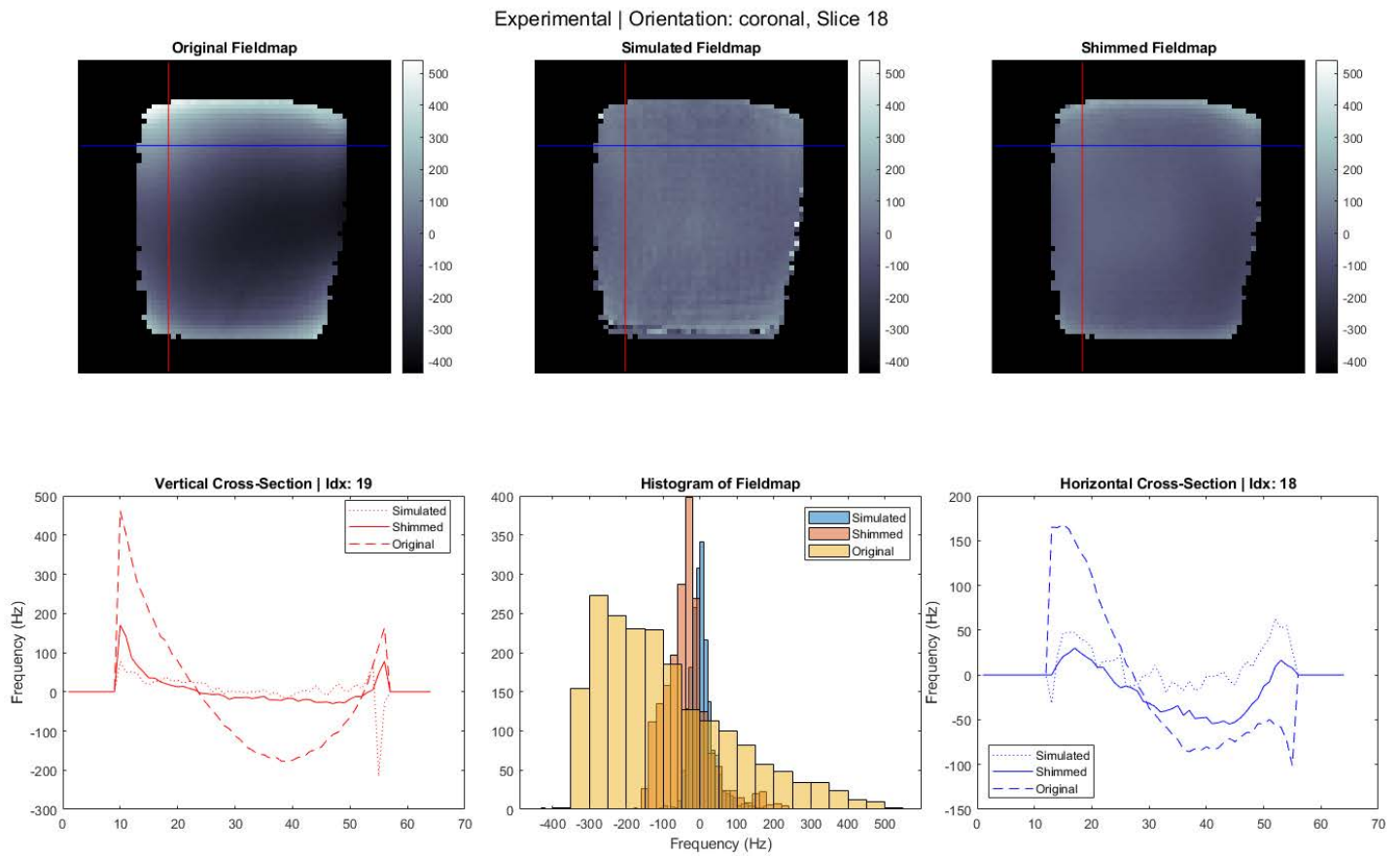


Figure 5.3: Experimental results for slice 18 (+3mm from center) in the coronal orientation. The overall deviation without the shim array was calculated to be 3.1179 ppm. The overall deviation was calculated to be 1.0663 ppm.

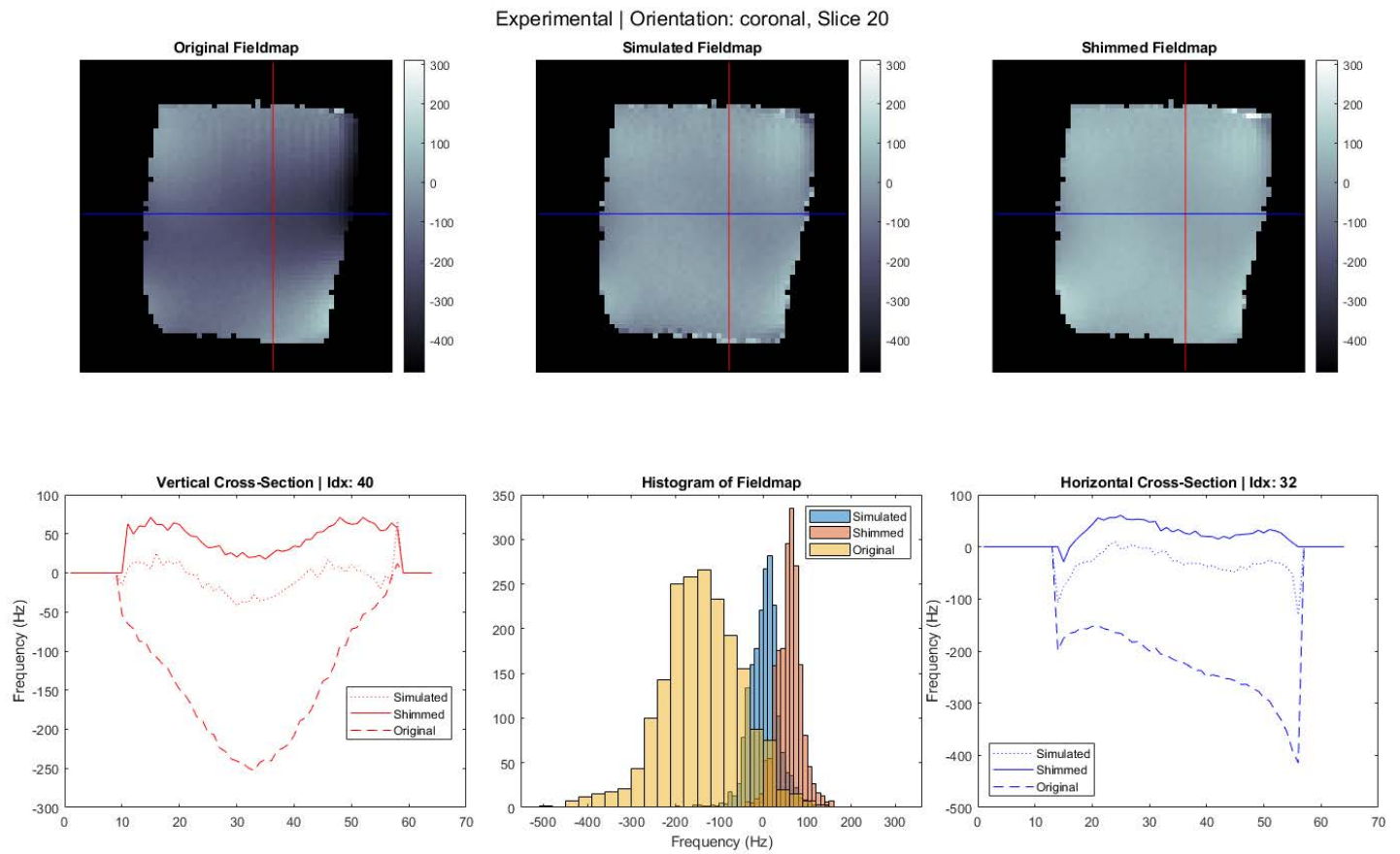


Figure 5.4: Experimental results for slice 20 (+6mm from center) in the coronal orientation. The overall deviation without the shim array was calculated to be 2.1243 ppm. The overall deviation with the shim array was calculated to be 0.7727 ppm.

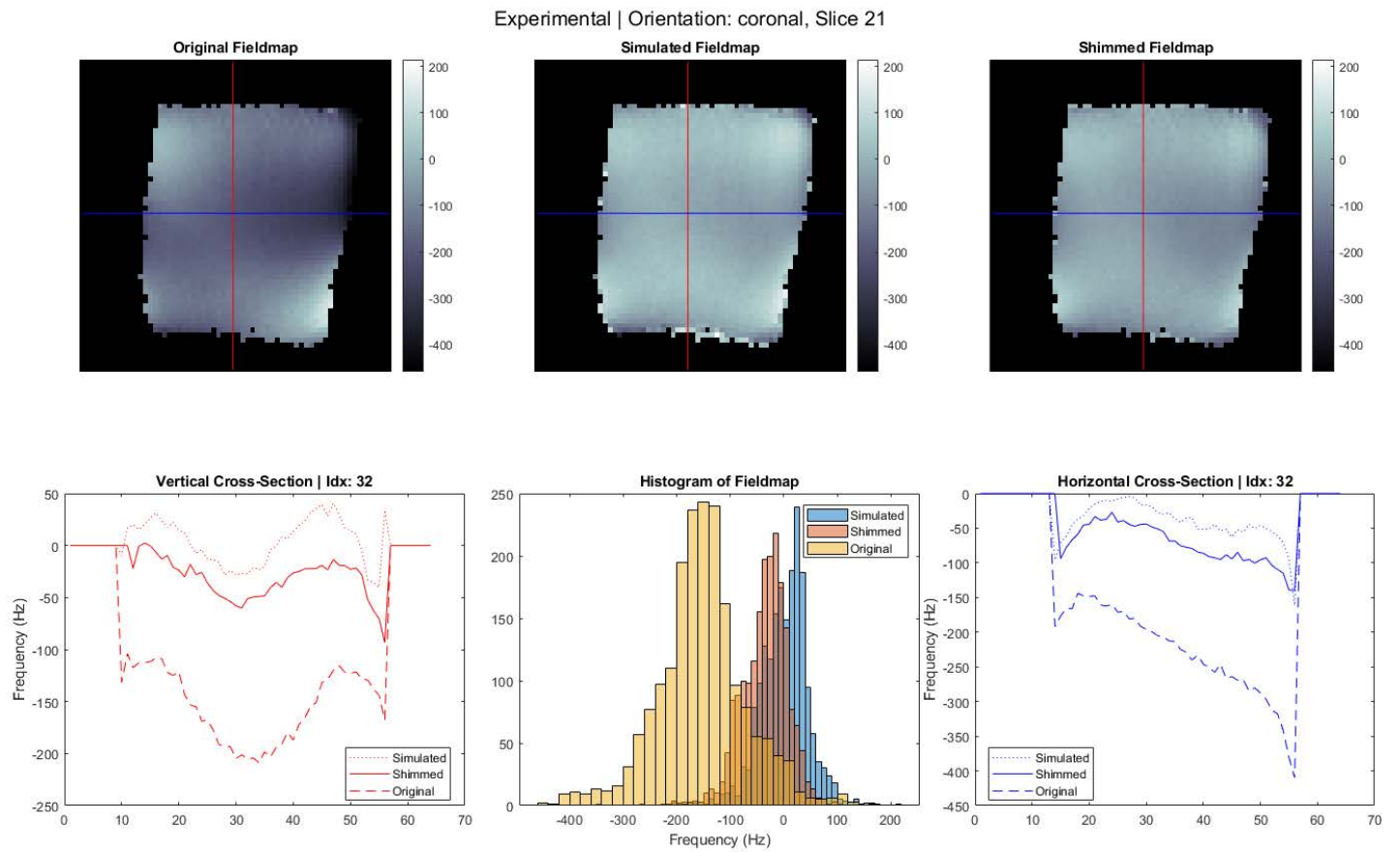


Figure 5.5: Experimental results for slice 21 (+7.5mm from center) in the coronal orientation. The overall deviation without the shim array was calculated to be 1.9430 ppm. The overall deviation was calculated to be 0.9981 ppm.

# Chapter 6

## Discussion

### 6.1 Conclusion

In this project, we presented a local  $B_0$  shim array for permanent magnet scanners that brought the shim coils closer to the subject to increase its field-to-current ratio. We fabricated the  $B_0$  shim array by hand using MR safe materials. Furthermore we demonstrated a targeted shimming procedure that reduced the overall field inhomogeneity for a target slice by a factor of 3. Our experimental setup optimized scan time through the use of tailored pulse sequences, minimized noise contribution through a novel current driver system, and automated the process of acquiring basis fieldmaps. Through our experimentation, we observe a significant increase in field homogeneity with minimal interference with the fundamental MR system.

### 6.2 Future Work

While our local shim array has been shown to be very successful at correcting the field inhomogeneities of target slices, the full potential of such a system lies more so in dynamic shimming. This would allow each slice of a volume to reap the benefits of a homogeneous field by quickly switching the shim solutions (current values and linear gradient amplitudes) throughout the duration of a scan. Theoretically, the current driver system was made specifically for such a task, but the codebase and supporting hardware were simply not made in time. A couple steps need to be taken to achieve dynamic shimming: (1) a gradient triggering signal must be read in by the Teensy microcontroller, (2) the shim solutions for the full volume must be precomputed, and (3) the current driver board must be synchronized with the pulse sequence.

Furthermore, most of our wiring for the shim array itself has been routed through the entrance of the magnet bore as an easy way to test whether the system works, but this is unsafe for clinical use. The sleeve which houses the subject has multiple live wires extending

from it and although the current they carry would not likely cause bodily harm, a new cable routing scheme would greatly clean up the system. This would come in the form of a new sleeve with a dedicated space for the shim array as well as a custom-machined back of the scanner which would house the wiring.

As discussed in the *Coil Configuration Optimization* section, the circular, uniform distribution of the 16 channel coil array is far from an optimal design. Due to simplicity and therefore ease of construction, this design was used as a proof of concept. However, one step to achieve even greater results than those presented in this thesis would be to construct a coil array via high precision fabrication (e.g. copper etching, flex PCBs, etc.) to match the coil configuration found by one of the optimization algorithms. From simulations, such a coil array has been demonstrated to be a significant improvement over the current design.

# Bibliography

- [1] Hui Han et al. “Integrated parallel reception, excitation, and shimming (iPRES)”. In: *Magnetic resonance in medicine* 70.1 (2013), pp. 241–247.
- [2] Nick Arango and Jason P Stockmann et al. “Open-source, low-cost, flexible, current feedback-controlled driver circuit for local B0 shim coils and other applications”. In: *ISMRM* (2016).
- [3] Matt A. Bernstein. *Handbook of MRI Pulse Sequences*. Academic Press, Sept. 2004. ISBN: 0120928612. URL: <https://www.xarg.org/ref/a/0120928612/>.
- [4] M A Brideson, L K Forbes, and S Crozier. “Winding patterns for biplanar MRI shim coils with rectangular and circular target-field regions”. In: *Measurement Science and Technology* 15.5 (Apr. 2004), pp. 1019–1025. DOI: 10.1088/0957-0233/15/5/035. URL: <https://doi.org/10.1088/0957-0233/15/5/035>.
- [5] B. Dorri, M.E. Vermilyea, and W.E. Toffolo. “Passive shimming of MR magnets: algorithm, hardware, and results”. In: *IEEE Transactions on Applied Superconductivity* 3.1 (1993), pp. 254–257. DOI: 10.1109/77.233719.
- [6] Jun-Jie Du et al. “A novel design methodology for active shim coil”. In: *Measurement Science and Technology* 23.8 (July 2012), p. 085502. DOI: 10.1088/0957-0233/23/8/085502. URL: <https://doi.org/10.1088/0957-0233/23/8/085502>.
- [7] Yang Gao et al. “A 16-channel AC/DC array coil for anesthetized monkey whole-brain imaging at 7T”. In: *NeuroImage* 207 (2020), pp. 116–396.
- [8] Douglas C. Giancoli. *Physics for Scientists and Engineers*. Englewood Cliffs, N.J.: Prentice Hall, 1989.
- [9] Michael Grant and Stephen Boyd. *CVX: Matlab software for disciplined convex programming, version 2.0*. 2013.
- [10] Michael Grant and Stephen Boyd. *Graph implementations for nonsmooth convex programs, Recent Advances in Learning and Control*. 2008.
- [11] Liming Hong and D. Zu. “Shimming Permanent Magnet of MRI Scanner”. In: *Piers Online* 3 (2007), pp. 859–864.

- [12] Paul Horowitz and Winfield Hill. *The art of electronics; 3rd ed.* Cambridge: Cambridge University Press, 2015. URL: <https://cds.cern.ch/record/1981307>.
- [13] Christoph Juchem et al. “Multicoil shimming of the mouse brain”. In: *Magnetic Resonance in Medicine* 66.3 (Mar. 2011), pp. 893–900. DOI: 10.1002/mrm.22850. URL: <https://doi.org/10.1002/mrm.22850>.
- [14] Xia Kong et al. “A novel passive shimming method for the correction of magnetic fields above the patient bed in MRI”. In: *Journal of Magnetic Resonance* 257 (2015), pp. 64–69. ISSN: 1090-7807. DOI: <https://doi.org/10.1016/j.jmr.2015.05.004>. URL: <https://www.sciencedirect.com/science/article/pii/S1090780715001123>.
- [15] Feng Liu et al. “A Hybrid Field-Harmonics Approach for Passive Shimming Design in MRI”. In: *IEEE Transactions on Applied Superconductivity* 21.2 (2011), pp. 60–67. DOI: 10.1109/TASC.2011.2112358.
- [16] Loic Queval. *BSmag toolbox user manual.* 2015.
- [17] Hector Sanchez Lopez et al. “Passive Shim Design and a Shimming Approach for Biplanar Permanent Magnetic Resonance Imaging Magnets”. In: *IEEE Transactions on Magnetics* 44.3 (2008), pp. 394–402. DOI: 10.1109/TMAG.2007.914770.
- [18] Jason P. Stockmann et al. “A 32-channel combined RF and B0 shim array for 3T brain imaging”. In: *Magnetic Resonance in Medicine* 75.1 (Feb. 2015), pp. 441–451. DOI: 10.1002/mrm.25587. URL: <https://doi.org/10.1002/mrm.25587>.
- [19] Sumit Tewari, Thomas O’Reilly, and Andrew Webb. “Improving the field homogeneity of fixed- and variable-diameter discrete Halbach magnet arrays for MRI via optimization of the angular magnetization distribution”. In: *Journal of Magnetic Resonance* 324 (2021), p. 106923. ISSN: 1090-7807. DOI: <https://doi.org/10.1016/j.jmr.2021.106923>. URL: <https://www.sciencedirect.com/science/article/pii/S1090780721000124>.
- [20] Sharon E. Ungersma et al. “Shim design using a linear programming algorithm”. In: *Magnetic Resonance in Medicine* 52.3 (2004), pp. 619–627. DOI: 10.1002/mrm.20176. URL: <https://doi.org/10.1002/mrm.20176>.
- [21] Qiuliang. Wang. *Practical design of magnetostatic structure using numerical simulation [electronic resource] / Qiuliang Wang.* eng. Hoboken, N.J: John Wiley Sons Inc., 2013. ISBN: 1-118-39815-7.
- [22] Peter T. While and Jan G. Korvink. “Designing MR Shim Arrays With Irregular Coil Geometry: Theoretical Considerations”. In: *IEEE Transactions on Biomedical Engineering* 61.6 (2014), pp. 1614–1620. DOI: 10.1109/TBME.2013.2293842.
- [23] Simone A. Winkler et al. “Gradient and shim technologies for ultra high field MRI”. In: *NeuroImage* 168 (2018). Neuroimaging with Ultra-high Field MRI: Present and Future, pp. 59–70. ISSN: 1053-8119. DOI: <https://doi.org/10.1016/j.neuroimage.2016.11.033>. URL: <https://www.sciencedirect.com/science/article/pii/S1053811916306498>.

- [24] Ziheng Zhang et al. “Magnetic resonance imaging of water content across the Nafion membrane in an operational PEM fuel cell”. In: *Journal of Magnetic Resonance* 193.2 (Aug. 2008), pp. 259–266. DOI: 10.1016/j.jmr.2008.05.005. URL: <https://doi.org/10.1016/j.jmr.2008.05.005>.